Using a microfluidic device that integrates microchannels with immobilized catalysts has been shown to improve the photocatalytic efficiency, thanks to its attractive features including a large surface-to-volume ratio, a short diffusion distance and a rapid mass transfer process of molecules from the solution to catalysts [6,7]. In addition, the immobilized catalysts do not require post-separation and recovery which are common for suspended catalysts, although their total surface area needs to be optimized. This kind of microfluidic reactors, as reported, has shown an efficiency which was two orders of magnitude higher than that of batch reactors [6-8].

There are still a few challenges to be addressed in order to apply microfluidic reactors in photocatalytic water purification. One is the sophisticated fabrication procedure arranged in the microscale dimensional domain. Polydimethylsiloxane (PDMS) is one popular material having been used as it is optically transparent, chemically inert and easy to be processed [7], but it has the risk of air inflow and may collapse due to its low elastic modulus [9]. Another challenge is the capacity or output of the microfluidic reactor. The small internal volume normally restricts the amount of water that can be treated [10]. Scaling-up and/or numbering-up methods are usually considered to solve this problem. While scaling-up may be difficult and potentially break down the microfluidic features, integrating a number of microfluidic reactors into one system, which is numbering-up, can multiply the output. For photocatalytic applications, however, each reactor needs to be exposed to the incident light, which complicates the numbering-up design. There are two major types of microfluidic reactors, namely, channel-based (microchannel reactor) and microchamber-based (microchamber reactor) [6-9]. The microchannel reactor is normally more efficient for catalytic applications, but its manufacturing is very complex, especially when many channels are piled into a large bundle [7]. Meanwhile, the incident light scattering or reflection between channels is an issue to be addressed during numbering-up of these reactors. On the other hand, the microchamber reactor is advantageous due to its larger output, less complex fabrication method and easier design for scaling-up or numbering-up and hence has a potential to be applied in the field of photocatalytic water purification or other catalytic reactions.

Some knowledge gaps remain on the design and operation of microchamber reactors for photocatalytic applications. For example, these influences of flow rates and microchamber geometries (e.g. height and catalyst shape) on the catalytic performance are not clear to date. The efficiency of microchamber reactors with varying heights of 100-800 um was reported to increase when the flow rate was changed from 25 to 600uL/min [6-9,11]. Beyond this range of flow rates, data are however lacking. Assuming that the flow rate is extremely high, the residence time of the polluted water within the reactor can be shorter than the time scale needed for photocatalyzed dye oxidation. Therefore, there should be a turning point from which the efficiency starts to decrease with flow rates. Investigation of this point will help to determine the optimal flow rate of the reactor. In addition, increasing the reactor height can increase the output but also extend the diffusion length which could result in a reduced efficiency. To understand how the reactor height affects the efficiency is a key step for scaling-up and determining the microchamber geometry with the optimized capacity and efficiency. To study the qualitative kinetics of the photocatalytic oxidation in microchamber reactors would help to address those issues.

Concerning the photocatalysts integrated with microchamber reactors, zinc oxide (ZnO) is less reported than titanium dioxide (TiO_2). ZnO has the advantages of lower cost and higher activity in the degradation of many kinds of dyes and bacteria [12-17], though it shows a comparatively lower stability. ZnO is able to be immobilized in the form of a nanoparticle thin film or vertically aligned nanorods. The cost-effective routes to fabricate ZnO thin film (seed layer) and nanorods are the sol-gel method and hydrothermal procedure, respectively [18,19]. It is important to choose a suitable catalyst state (seed layer or nanorods) for improving the efficiency of a microchamber reactor. The ZnO nanorods are deemed to be more efficient thanks to the comparatively higher surface area. The performance of ZnO nanorods, however, has been reported to be better or worse than the thin film prepared from various methods [20-24]. In the case where the thin film was more active, it was attributed to the higher surface-to-volume ratio and better (002) orientation [21]. When the nanorods performed better, the authors referred it to the joint effects of their higher surface area,

better wettability, larger roughness and smaller band gap energy [24]. A comparative study of the ZnO seed layer and nanorods is necessary not only for the design of microchamber reactors but also for a comprehensive understanding of their different activities.

In this work, we developed a unique design of microchamber reactors to accommodate the photocatalytic activities of ZnO nanoparticles and nanorods. The fabrication method was simple, the reactor height was readily controlled by using different spacers, and the reactor was ready for scaling-up and numbering-up. The ZnO nanoparticle seed layer and vertically aligned nanorods with different lengths were fabricated directly on the bottom wall of these reactors, which was dismountable and renewable. A comprehensive understanding of their photocatalytic performances was achieved by extensive characterizations of their microstructures and reaction constants. The kinetics of photocatalytic oxidation in microchamber reactors was qualitatively determined, and the effects of flow rates and reactor heights were also demonstrated.

2. Experimental

2.1 Preparation and characterization of the ZnO seed layer and nanorods

The ZnO seed layer was produced by a sol-gel procedure and the vertically aligned nanorods were hydrothermally grown on seed layer coated glass substrates [19]. The growth was conducted for 2h, 4h or 6h to achieve ZnO nanorods with different lengths, denoted here as nanorods_2h, nanorods_4h and nanorods_6h in the following text. The details are shown in supplementary materials.

The morphologies and microstructures of the ZnO seed layer and nanorods were examined by using an atomic force microscopy (AFM, Multimode^{TM} SPM, Digital Instruments) in a tap mode, a X-ray diffractometer (XRD, X'pert Pro MRD, PANalytical) and a scanning electron microscope (SEM, Zeiss ULTRA Plus). An ultraviolet-visible (UV-Visible) spectrometer was employed to measure the transmittance of the ZnO samples in a wavelength range of 200-500nm. Photoluminescent (PL) measurement (Edinburg Instruments) in a wave length range of 350-850nm with a step of 1nm and a dwell time of 0.5 second was performed for the ZnO samples at room temperature. The PL was excited by a 330nm line of He-Cd laser.

2.2 Design of a microchamber reactor integrated with the ZnO samples

A sandwiched configuration of a microchamber reactor was developed for the photocatalytic reactions. As shown in Fig. 1, it was assembled by seven layers: from the bottom to the top, (1) a bottom aluminum base; (2) a lower polymethyl methacrylate (PMMA) base; (3) a ZnO seed layer or nanorods coated glass slide; (4) a silicon rubber gasket, whose thickness was the reactor height and could be flexibly adjusted from 127μm up to 5mm in this work; (5) a bare glass slide exposed to the incident light; (6) an upper PMMA plate; and (7) a top aluminum plate. Both the upper PMMA plate and the top aluminum plate were produced with a rectangular opening (59mm×10mm) right through their whole thicknesses, allowing the external incident light reaching onto the bare glass slide and penetrating to the interior solution. Moreover, each of these two layers and the bare glass slide were drilled with two holes that facilitated the inflow of the MO solution from one side and the outflow after the photocatalytic reaction from the other side. These holes on both sides were aligned coaxially and connected as well as sealed by using O-rings. Twenty screws were fastened between the top and the bottom aluminum layers, without interfering with the middle five layers, to seal the system. Note that although there was a slight squeezing deformation of the gasket due to the compression, it did not change its thickness too much (< 5%).

2.3. Evaluation of photocatalytic performances of the ZnO samples in the batch reactor and microchamber reactors

The aqueous MO solution (5ppm) was chosen as a model polluted water. For the batch reactor, one sample of the ZnO seed layer or nanorods was immersed into 15mL MO solution stirred by a magnetic bar at 300rpm. Before irradiation, the MO solution had been stirred for half an hour to ensure adequate absorption of the dye onto the catalyst surface. Then the reactor was located and irradiated under the center of an area source of UV light with a power of 100W, a diameter of around 18cm and a wavelength of 365nm. ZnO has a band gap of 3.37 eV, which corresponds to emission in the UV region (<375nm). Considering UV with a larger wavelength is more in solar UV, we chose 365nm rather than other common commercial UV lamps of

320nm or 350nm. The UV intensity on the sample was not homogeneous due to the features of an area light source and distributed in the range of 5-16mW/cm^2. During the irradiation, every 30 minutes the absorption spectrum of the MO solution was measured using a UV-Visible spectrometer. Its absorbance at a wavelength of 464nm was proportional to its concentration and decreased with the irradiation time. Then the degradation rate of MO and the efficiency of the ZnO samples in the batch reactor were determined. In addition, the MO solution in the batch reactor without ZnO catalysts was irradiated by UV to study the photolysis of MO.
The microchamber reactor was irradiated by the same UV source. The inlet was connected with a syringe via tubing driven by a syringe pump to control the flow rate. The MO solution was injected into the reactor at different flow rates ranging from 50 to 1400uL/min. The degraded MO solution was collected at the outlet. Note that the whole system was in a continuous operation for around twenty minutes before any sample was collected. This waiting time was to ensure the flow rate got stable. In addition, any bubble in the tubing had to be avoided, as it might not be eliminated once introduced into the chamber. By comparing the UV-Visible absorbance of the original MO solution and the collected sample, the efficiency of the ZnO samples in microchamber reactors was obtained. Additionally, the microchamber reactor with the MO solution but without ZnO catalysts was irradiated by UV, where the photolysis of MO was too little to be detected as the residence time of the MO solution was as short as several to tens of minutes.

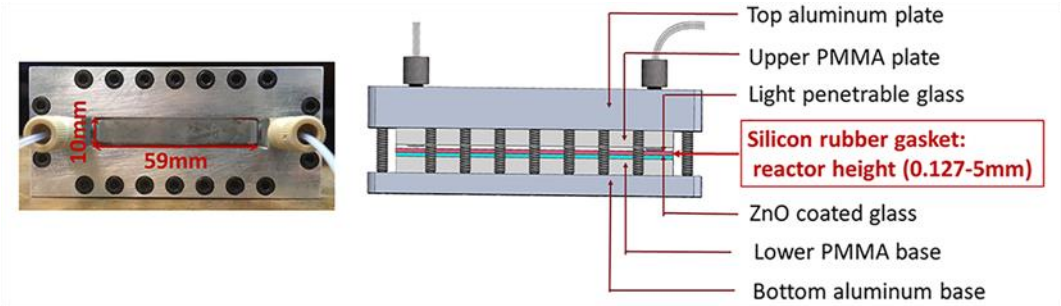

Figure 1. A photo of top view (left) and an assembly image of the microchamber reactor (right).

3. Results and discussion

3.1 Characterization of the ZnO samples

For photocatalytic reactions, the structure and surface properties of photocatalysts are of especial significance. The XRD patterns in Fig. S1 revealed a strong preferential orientation of ZnO in c-axis perpendicular to the substrate, which is common for hydrothermally grown ZnO. The penetration length (where the intensity falls to ~37% of the original value) of UV light at 365nm into ZnO is ~40nm [25]. Based on that, UV light is estimated to penetrate into the top surface of ZnO by around 100nm before dropping to 0. Beyond that distance, the interior part of the ZnO samples is not excited to produce e/h pairs. In other words, only the material with a thickness of several tens of nanometers is effective. Compared to the surface properties of the seed layer, the nanorods presented a larger overall surface area, higher surface roughness (Fig. S2), higher UV absorption, smaller band gap energy (Fig. S3) and more defects (which leads to a lower crystal quality) (Fig. S4). The length of the nanorods_2h, _4h and _6h was ~1μm, 2-2.5μm and 3-4μm (Fig. 2), respectively. The details are shown in supplementary materials.

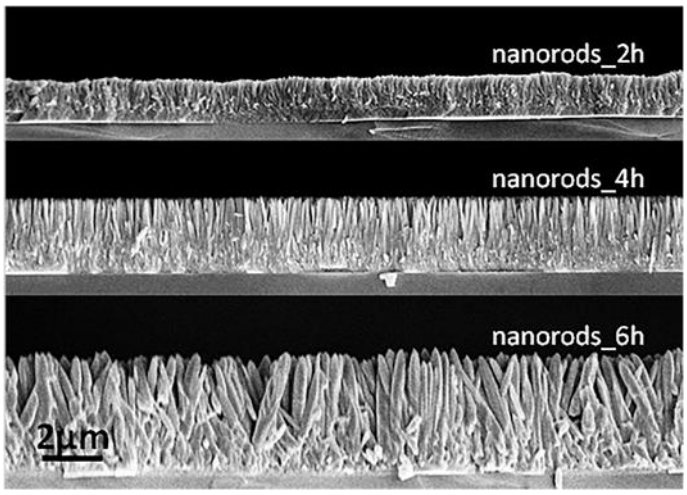

Figure 2. SEM images of the longitudinal cross section of the ZnO nanorods_2h, _4h and _6h.

3.2 Photocatalytic performances of the ZnO samples in the batch reactor

The photocatalytic efficiency of the ZnO seed layer and nanorods in the batch reactor is presented in Fig. 3. The uncertainties here and in the following figures were determined using the standard deviation. The photolysis of MO under the experimental conditions in this work was very little, ~5% after 4 hours' irradiation, and ignored in the photocatalytic results. The ZnO seed layer, nanorods_4h and _6h performed similarly and better than the nanorods_2h. From Fig. 3a one can notice a continuous degradation of MO under the UV irradiation. After 4 hours, 97% of MO was decomposed by using the seed layer, nanorods_4h and _6h. 90% of MO was degraded by the nanorods_2h. Fig. 3b presents the fitting of $-\ln(C/C_0)$ versus irradiation time where C is the concentration of the MO solution after the UV irradiation and C_0 is the original concentration. $-\ln(C/C_0)$ was a linear function of the reaction time, matching the first order reaction law. The slope was used to calculate the reaction constant K (min^{-1}), representing the degradation rate of MO or the efficiency of the ZnO samples in the batch reactor. The K of the seed layer, nanorods _2h, _4h and _6h was 0.014±0.001, 0.010±0.001, 0.015±0.001 and 0.015±0.001, respectively.

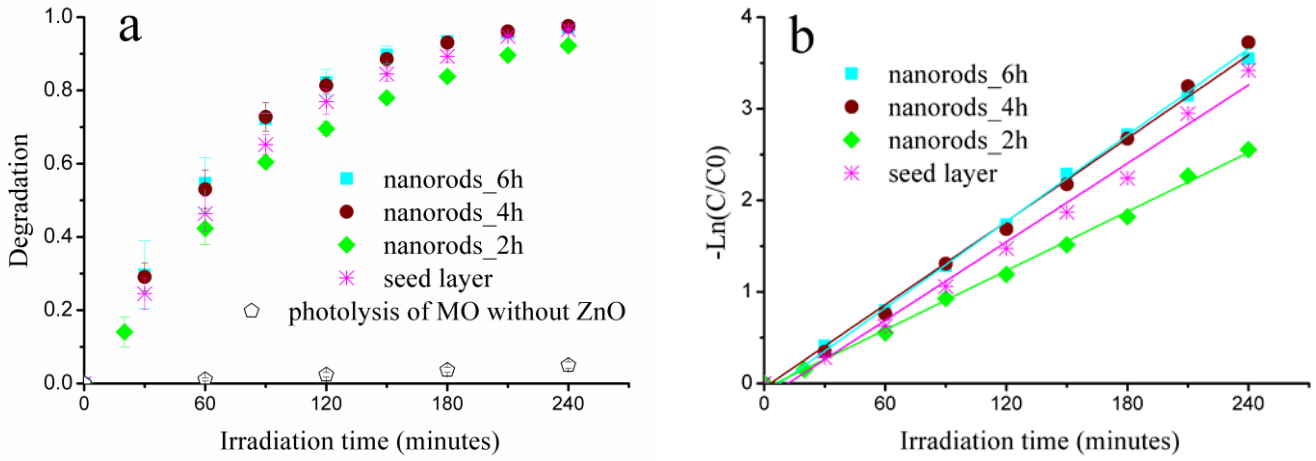

Figure 3. Photocatalytic degradation of MO under UV light by using the ZnO samples in the batch reactor (a) and plots of $-\ln(C/C_0)$ versus irradiation time (b).

That observation of the worse (nanaorods_2h) or similar (_4h and _6h) activities of nanorods, compared with the seed layer, was not expected, considering that the nanorods had the joint effects of larger surface area, larger roughness and smaller band gap energy, which were responsible for the better behavior of the nanorods in ref. [24]. The most possible explanation of our observation was that the low crystal quality (too many defects) of the nanorods traded off the aforementioned joint effects. Separation of e/h pairs is a key factor to

achieve a good activity, as the recombination probability is high [1]. A high crystallinity which leads to better transportation/separation of e/h pairs and more surface defects that act as active reaction centers are both beneficial for improving the photocatalytic efficiency [1,5,26-28]. But a comparatively large amount of defects reduces the crystallinity. In our case that all the samples possessed a considerable number of defects, the crystal quality played a more significant role in determining the efficiency. This hypothesis was supported by the annealed nanorods_6h (500^{o}C for 1 hour in air), which showed an improved crystallinity and resulted in a higher photocatalytic activity (0.019) than the as-produced nanorods_6h (Fig. S4 and S5).

Another noteworthy result is that the nanorods_4h and _6h with different lengths exhibited the comparable activity. Similarly Z. Liu et al. reported that TiO_2 nanotubes with a length of 12um and 17um were equally active [29]. It was likely caused by the light trapping or MO trapping among the long and dense nanorods. The UV light could be absorbed or obstructed by the upper parts of the nanorods, leaving their lower parts unreachable. In other words, there is a "UV shadow". Moreover, negatively charged MO molecules that are adsorbed onto the top parts of nanorods become a barrier for further adsorption of MO molecules onto the deep parts, which causes a "MO shadow". Due to the existence of the UV shadow and MO shadow, the performance of the nanorods increased firstly with the length due to the enlarged surface area (nanorods_4h > nanorods_2h), but became stabilized when the nanorods became longer and/or denser (nanorods_4h = nanorods_6h).

3.3 Photocatalytic performances of the ZnO samples in microchamber reactors

The photocatalytic efficiency of the ZnO seed layer was evaluated in microchamber reactors with a height of 0.127-5mm by applying flow rates of 50-1400uL/min. When the chamber height was at the millimeter scale (1-5mm), the flow rate was set to a small range of 50-600uL/min. Increasing the flow rate was found to cause a very small change in the concentration of the MO solution after flowing out of the reactor, which was out of the measurable range of the UV-Vis spectrometer. The effects of flow rates, reactor heights and the initial MO concentration on the reaction constant K (min^{-1}), which represents the efficiency, are shown in Fig. 4. The K was defined as $-(\ln C/C_0)/t$, where C_0 is the initial MO concentration, C is the MO concentration of the solution flowing out of the reactor and t is the residence time (the volume of the reactor divided by the flow rate). It is clearly demonstrated that the K of the microchamber reactor was one to two orders of magnitude higher than that of the batch reactor (0.015). Moreover, the K curve possessed a plateau with the increase of the flow rate (Fig. 4a) and exhibited an exponentially decreasing function of the chamber height (Fig. 4c). The chamber height influenced the efficiency much greater than the flow rate did. In addition, the K curve declined with the increase of the initial MO concentration (Fig. 4d).

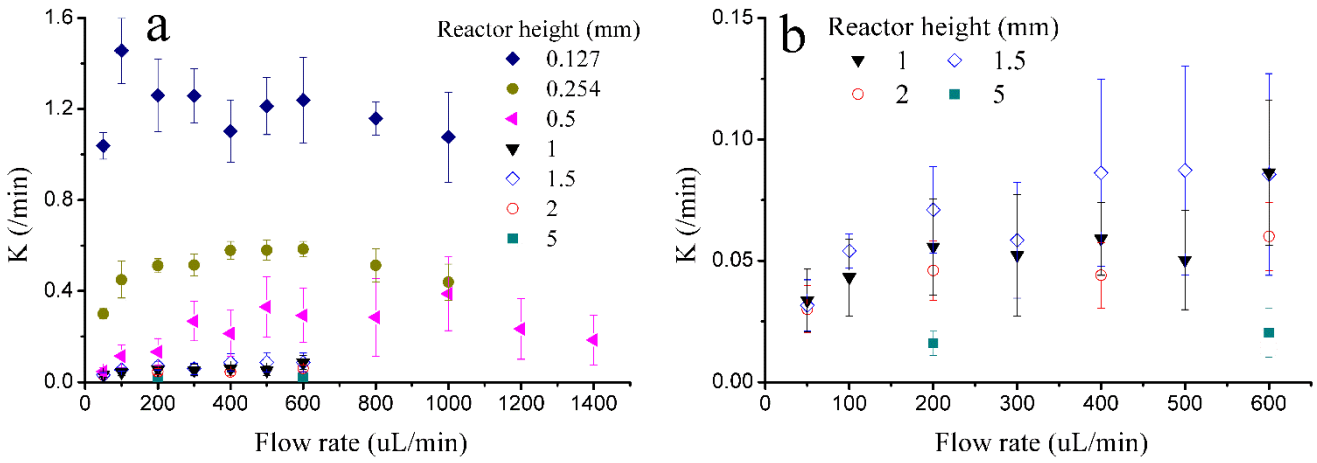

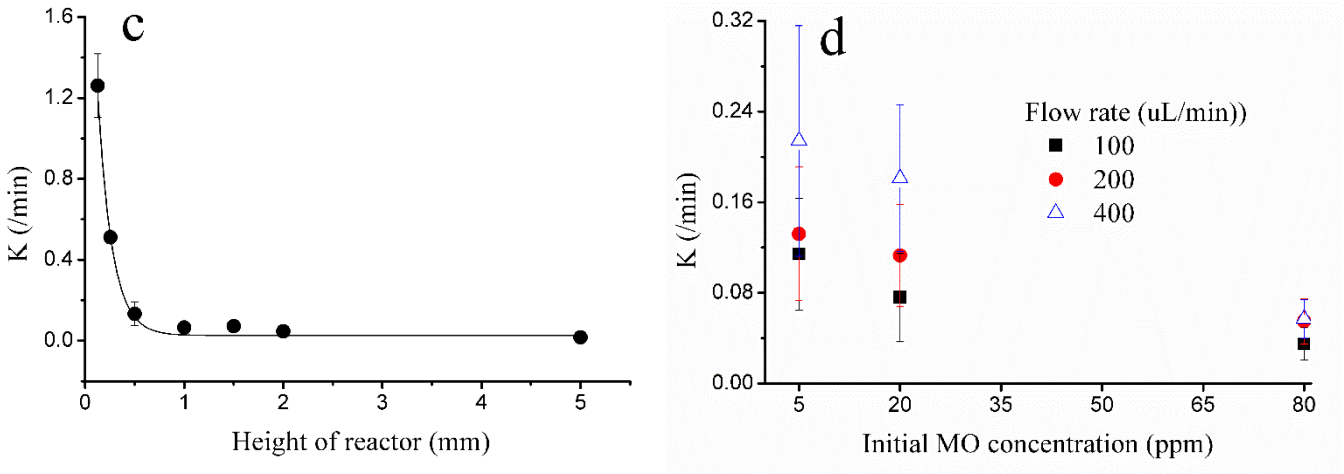

Figure 4. Plots of the reaction constant of the ZnO seed layer in microchamber reactors versus flow rates (a, b), versus reactor heights at a certain flow rate of 200μL/min (c) and versus the initial MO concentration at a certain flow rate of 100, 200 and 400μL/min (d).

The photocatalytic performances of the ZnO seed layer and nanorods were compared in the microchamber reactor with a height of 0.5mm by applying flow rates of 50-1000uL/min. The *K* of each sample versus flow rates is presented in Fig. 5. The efficiency of the samples was pretty similar and the minor difference was almost within the scope of the error bar. However, the batch reactor screened out the nanorods_2h, which showed a slightly lower efficiency than the other samples. That means the microchamber reactor may not differentiate photocatalysts which have slightly different photocatalytic properties.

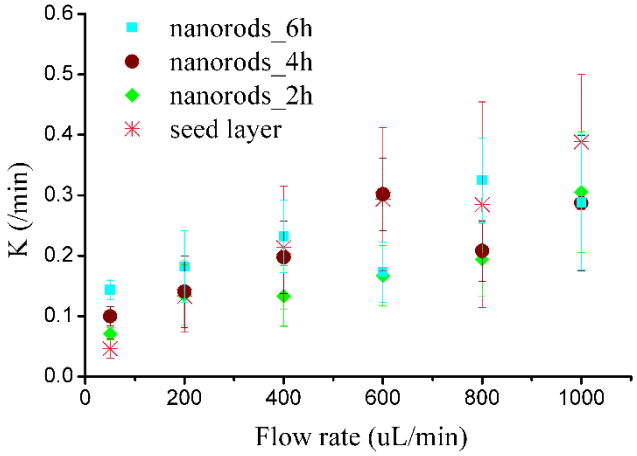

Figure 5. Plots of the reaction constant of the ZnO seed layer and nanorods versus flow rates in the microchamber reactor with a height of 0.5mm.

In this work, the accuracy of the derived reaction constant within the microchamber reactor was limited by three factors, which were the major causes of the relatively large error bars presented in the figures. The first factor was associated with the ductile spacer of silicon rubber gaskets. When the soft spacer was compressed during the assembly of the sandwiched reactor, it was slightly deformed. In different reactors, the spacers could end up with slightly different rectangle-like shapes, resulting in uncertainties. Another factor was the dead volume in the reactor, which was referred to the stagnant liquid that is randomly attached to the inner wall of the reactor due to surface tension. The heterogeneity between the dead volume and the flowing solution would generate uncertainties. The third factor was related to the measurement error of the MO concentration which could lead to a big variation of the reaction constant (K=-ln (C/C_0) /t) through error

propagation. This uncertainty was especially considerable, when both the reactor height was greater than 1mm and the flow rate became larger than 200uL/min. In these conditions, the concentration decrease (C_0-C) was as small as <10% of the original concentration, which was near the system error of the UV-Vis spectrometer.

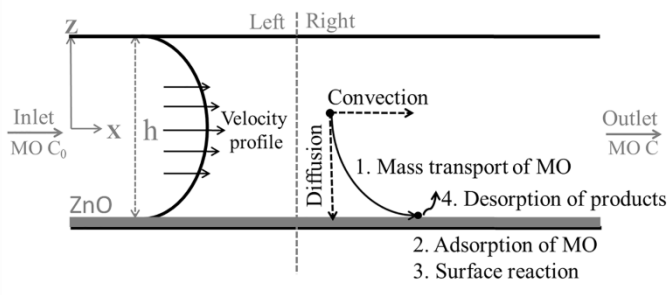

Figure 6. A schematic diagram of the flow pattern (left) and procedures of the photocatalytic oxidation (right) in microchamber reactors.

The photocatalytic oxidation kinetics in microchamber reactors involves flow-pattern-relevant mass transport followed by a sequence of adsorption, surface reaction and desorption as shown in Fig. 6 (right). There is a laminar flow in the reactor, since the Reynolds numbers in all experiments are in the range of 0.1-2.6. The mass transport of MO to the bottom where catalysts are located is achieved mainly by diffusion. Considering the first two steps of mass transport and adsorption, in ref. [30,31] an expression of the initial rate constant k_A (mm/min) of adsorbates being adsorbed onto the immobilized adsorbents in a slit (microchamber) was proposed for laminar flows. The k_A was defined as $k_A C = \mathrm{d}\Gamma/\mathrm{d}t_{t\to 0}$, where Γ (mg/m^2) is the adsorption amount per area, t (min) is the adsorption time, C (mg/L or ppm) is the adsorbate concentration and the kinetic order is one. The k_A is a function of the kinetic adsorption rate constant k_a (mm/min) and the mass transport controlled Lévêque constant k_{Lev} (mm/min). The expression of $k_A^{-1}=k_a^{-1}+k_{Lev}^{-1}$ is the simplest approximation. Ref. [30] can be referred to for deriving a more accurate and complex function of k_A. The k_a is related to the energy barrier of adsorption. The k_a of MO being adsorbed onto ZnO in this work is assumed to be inversely proportional to the initial MO concentration C_0, based on the fact that the k_a of MO being adsorbed onto Al_2O_3 supported ZnO versus $1/C_0$ was roughly linear with the correlation constant being 0.994 in conditions of C_0<150ppm [32]. This agrees with that a higher MO concentration causes a higher mass transfer resistance [32]. Then k_a is roughly calculated by $k_a = a/C_0$, where a is a constant. The k_{Lev} corresponds to a fully mass transport controlled adsorption. The expression is $k_{Lev}(x)=0.538(D^2\gamma/x)^{1/3}$, where D (mm^2/min) is diffusion coefficient of the adsorbate, x is the distance from the entrance and γ (/min) is shear rate at the bottom wall where the adsorption occurs [30,31,33]. The average value over the reactor length L (mm) is $k_{Lev}=0.808(D^2\gamma/L)^{1/3}$ [30]. The velocity profile of the laminar flow in a slit is parabolic along the chamber height as shown in Fig. 6 (left) and relevant expressions are as follows [34]:

$$V(Z) = \frac{\nabla P}{2\eta}\left(\frac{h}{2} - Z\right)\left(\frac{h}{2} + Z\right) \tag{1}$$

$$\nabla P = \frac{12\eta Q}{wh^3} \tag{2}$$

$$\gamma = \frac{\mathrm{d}V}{\mathrm{d}Z} = \frac{6Q}{wh^2} \quad \left(Z = \frac{h}{2}\right) \tag{3}$$

where V is velocity (mm/min), ∇P is pressure drop (Pa/mm), h is the reactor height (mm), w is the chamber width (mm), Q is the volume flow rate (uL/min) and η is the viscosity of the flowing solution (Pa • min). By substitution, the expression of the adsorption rate constant is obtained as follows:

$$k_A = \frac{1}{\frac{Co}{a} + \frac{L^{1/3}w^{1/3}h^{2/3}}{0.808D^{2/3}6^{1/3}Q^{1/3}}} = \frac{1}{\frac{Co}{a} + \frac{bh^{2/3}}{Q^{1/3}}} \tag{4}$$

where b is a constant determined by w, L and D. The k_A needs to be transformed in order to describe the MO concentration decrease caused by adsorption. The transformation is presented as follows:

$$\frac{\partial C}{\partial t} = \frac{\partial \frac{\Gamma s}{sh}}{\partial t} = \frac{1}{h}\frac{\partial \Gamma}{\partial t} = \frac{1}{h}k_A C_0 = K_A C_0 \quad (K_A = \frac{1}{h}k_A) \tag{5}$$

where s (mm^2) is the surface area of the adsorbent ZnO, Γs is the adsorption amount, sh is the volume of the MO solution, $\Gamma s/sh$ is the MO concentration change after adsorption, and K_A (/min) is the transformed adsorption rate constant. By combining equation (4) and (5), the expression of K_A is obtained as follows.

$$K_A = \frac{k_A}{h} = \frac{1}{\frac{hCo}{a} + \frac{L^{1/3}w^{1/3}h^{5/3}}{0.808D^{2/3}6^{1/3}Q^{1/3}}} = \frac{1}{\frac{hCo}{a} + \frac{bh^{5/3}}{Q^{1/3}}} \tag{6}$$

In the microchamber reactor, a rate determining step could be the surface photocatalytic reaction or mass transport relevant adsorption, assuming desorption of products is very fast (fourth step in Fig. 6 right). If the surface reaction is the rate limiting process, the overall reaction rate K should not change much with varying flow rates, which doesn't agree with the experimental data (Fig. 4a, b). Therefore, the mass transport related adsorption is more likely to be the rate determining step. This implies that any adsorbed MO molecules would react instantly and the surface adsorption is away from equilibrium. The K is a function of the adsorption rate constant K_A (not adsorption equilibrium constant) and active center coverage on the surface of ZnO θ_{ZnO} as shown in the following [35].

$$K=K_A\theta_{ZnO.} \tag{7}$$

The θ_{ZnO} is determined by properties of the ZnO samples and the UV intensity. With the same UV irradiation, the efficiency of microchamber reactors is controlled by the reactor geometry (e.g. h), the flow rate, the MO concentration, and catalyst properties. In addition, the overall reaction order is the order of adsorption, which is one [32]. Therefore, the definition of the experimental reaction constant K ($-(\ln C/C_0)/t$) is reasonable.

As for the efficiency of the ZnO seed layer in microchamber reactors with various heights, if the slight UV intensity reduces caused by the adsorption of the flowing MO solution are ignored, θ_{ZnO} is a constant. The K is described as follows:

$$K = K_A\theta_{ZnO} = \frac{1}{\frac{hCo}{a} + \frac{bh^{5/3}}{Q^{1/3}}}\theta_{ZnO} = \frac{1}{\frac{hCo}{A} + \frac{Bh^{5/3}}{Q^{1/3}}} \tag{8}$$

where A and B are constants derived from a, b, and θ_{ZnO}. According to equation (8), the reaction constant is enhanced with increasing the flow rate but decreases with the chamber height as well as the initial MO concentration. And the effect of the reactor height is especially significant since it has the biggest exponent (5/3). Those are in principle consistent with the experimental results shown in Fig. 4. As for the second stage in Fig. 4a where the efficiency started to decline with flow rates, it was possibly due to the too short residence time which might be even smaller than the time scale of adsorption or reaction. The time scale calculated according to the plateaus in Fig. 4a was around 0.25-0.5s. Therefore, the proposed kinetics is applicable in a certain range of flow rates. Beyond that range an additional factor of residence time should be taken into account.

To further verify the reliability and limitations of the above kinetics, in Fig. 7 the curves (dotted lines) of equation (8) substituted by fitting numbers of A and B were compared with the experimental results (scatters) when the K increased with flow rates (first stage of Fig. 4a, b). The A and B in equation (8) were fitted to be 2 and 80 by the experimental data of reactors with a height of 0.127-1mm. The equation fits the experiments well in a wide MO concentration range of 5-80 ppm in Fig. 7a and c. In Fig.7c, the fitted lines do not exactly match the average experimental values, but fall within the error bar. When the reactor is higher than 1mm (Fig. 7b), the experimental rate constant is a little larger than the value obtained by the fitted equation. The adsorption model used to derive the kinetics describes the initial adsorption rate constant when the adsorption time approaches zero. The adsorption constant may vary with time. The experimental data are average values over the whole residence time. This time factor could be different in microchamber reactors with different heights, since the residence time is different. In addition, a simplest model of adsorption is

referred to, which restricts the precision. In the model, k_a is assumed to be in an inversely linear relationship with the MO concentration for simplification. The inverse function is likely not to be exactly linear. Furthermore, the formula of the K doesn't involve desorption of photocatalytic products which may affect active center coverage θ_{ZnO}. In view of these constraints, this kinetic equation is proposed to be applied qualitatively. The fitted values of A and B (2 and 80) are for the comparison of experiments and the equation, yet probably not the accurate physical values. Overall, the proposed kinetics qualitatively predicts and explains the variation trend of the K with Q, h, and C_0 in experiments.

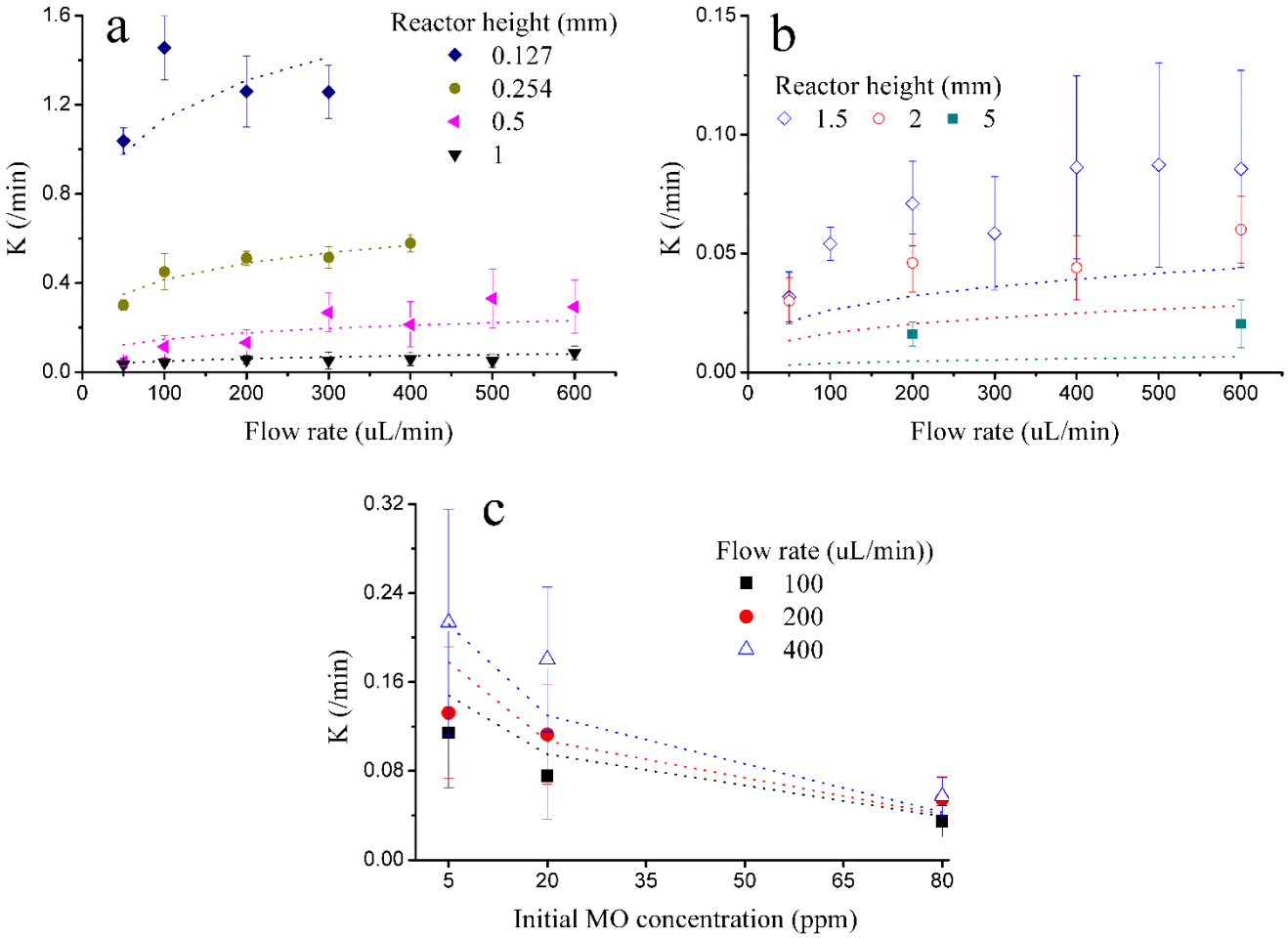

Figure 7. Plots of the reaction rate versus flow rates by using microchamber reactors with a height of 0.127-1mm (a) and with a height of 1.5-5mm (b), and the plot of the reaction rate versus the initial MO concentration by using the microchamber reactor with a height of 0.5mm (c). The dotted lines and the scatters are based on the data of seed layer obtained by the proposed kinetics and by experiments, respectively.

The proposed qualitative kinetics can explain the fact that the ZnO samples, which showed different performances in the batch reactor (nanorods_2h was worse than the others), performed similarly in a microchamber reactor. In microchamber reactors, mass transport related adsorption is a determining step, and the reaction constant is associated with the reactor geometry, the flow rate and ZnO properties (equation 8), resulting in a diluted impact of ZnO properties. The impact of ZnO properties might be even covered by the limited precision of our microfluidic measurements. In the well stirred batch reactor, the adsorption equilibrium is reached before photocatalytic reactions occur, as the turbulent mixing eliminate the mass transport effect. The kinetics is expressed as $K=K_{ads}K_R\theta_{ZnO}$, where K_R is the surface reaction constant (mg/L/min), and K_{ads} is the adsorption equilibrium coefficient (L/mg) [36]. All parameters are related to ZnO properties. Therefore, only the batch reactor screened out nanorods_2h with a slightly lower efficiency. The microfluidic devices have been proposed to fast screen catalysts. For this application, the precision of the device, such as the flow rate control and the reactor geometer, has to be in a very high level.

In consideration of the output of reactors, which is concerned in some practical applications, the nominal capacity is proposed here as another significant parameter except for the reaction constant. The nominal capacity (mL/min/m^2) of a reactor in this work was defined as the volume of 5ppm MO solution, which can be treated to a degradation of 97% within 1 min by using the ZnO seed layer with an area of 1m^2. In our batch reactor, 15mL MO solution was degraded by 97% in 240min and the area of the seed layer was 1875mm^2 (75mm×25mm). The nominal capacity was 33 mL/min/m^2 (15mL/240min/1875×$10^{-6}$$m^2$). After flowing out of the microchamber reactor, the degradation of the MO solution did not reach 97%. Assuming that this once-treated MO solution circulates the microchamber reactor for several more times until the degradation reaches 97%, the total time (t) could be calculated by the expression: K= -ln[(1-97%)C_0/C_0]/t, where K was obtained by experiments as shown in Fig. 4. Then the nominal capacity of the microchamber reactor was calculated by microchamber volume divided by t and the area of the ZnO seed layer, and is presented in Table 1. The bold font is to highlight the nominal capacity which is larger than that of the batch reactor. A higher reaction constant did not necessarily correspond to a larger capacity. For example, as shown in red font in Table 1, the reactor with a height of 0.127mm and a flow rate of 400uL/min had a higher reaction constant and a smaller capacity, compared to the reactor with a height of 0.5mm and a flow rate of 1000uL/min. To design a microchamber reactor, the reaction constant and the nominal capacity are two evaluation criteria. For some small-volume applications such as materials screening and detection, the reaction constant is dominant. In other practical uses, e.g. photocatalytic water purification, the capacity has to be considered, where a specific reactor height and a certain flow rate should be collaborated.

Table 1. The nominal capacity of microchamber reactors.

	Microchamber reactors with different heights (mm)						
	0.127	0.254	0.5	1	1.5	2	5
Flow rates (uL/min)	The nominal capacity (mL/min/m^2)						
50	**38**	22	6	8	11	17	
100	**53**	**33**	14	11	18		
200	**46**	**37**	16	14	24	26	23
300	**46**	**37**	32	13	20		
400	**40**$_{(K=1.103)}$	**42**	26	15	29	25	
500	**44**	**42**	**40**	12	30		
600	**45**	**42**	**35**	14	29	32	29
800	**42**	**37**	**34**				
1000	**39**	32	**47**$_{(K=0.388)}$				
1200			28				
1400			22				

4. Conclusions

In this work, the ZnO nanoparticle seeding layer and nanorods were fabricated and integrated into a seven-layer sandwiched microfluidic chamber. The photocatalytic efficiency of microchamber reactors with a height of 0.127-5mm was found to be one to two orders of magnitude higher than that of the batch reactor. The qualitative kinetics of photocatalytic oxidation in microchamber reactors was determined. The rate limiting step was suggested to be the mass transport relevant adsorption (the adsorption rate was controlled both by the mass transport and properties of adsorbates/adsorbents). The rate constant was elucidated as a function of the flow rate, the reactor geometry, the initial MO concentration as well as properties of photocatalysts. Compared to a batch reactor, the impacts of photocatalyst properties on the reaction constant were diluted by mass transport effects. For the ZnO samples with a large amount of structural defects, their

crystalline quality was of significance for determining the photocatalytic efficiency. The proposed qualitative kinetics and the experimental data are of great assistance to the design, optimization and scaling-up of microchamber reactors for different purposes. For practical uses (e.g. water purification) where the output is essential, a certain flow rate needs to be optimized with a specific reactor height. If the microchamber reactor is designed to fast screen catalysts, a high level of precision has to be obtained to avoid the uncertainties of the flow rate and the reactor geometry covering the difference of catalysts.

Acknowledgements

This work is kindly supported by the Emerging Energy Research (LEER) group and Microfluidics Laboratory, University of Waterloo. The authors would like to thank Prof. S. Sivoththaman and Dr. B. Sadeghimakki very much for their help on the PL measurements and transmittance tests.

References

[1] X. Zhang, J. Qin, Y. Xue, P. Yu, B. Zhang, L. Wang, R. Liu, Effect of aspect ratio and surface defects on the photocatalytic activity of ZnO nanorods, Sci. Rep. 2014, 4, Article number: 4596.

[2] M.N. Chong, B. Jin, C.W.K. Chow, C. Saint, Recent developments in photocatalytic water treatment technology: A review, Water Res. 44 (2010) 2997–3027.

[3] N. Wang, X. Zhang, Y. Wang, W. Yu, H.L.W. Chan, Microfluidic reactors for photocatalytic water purification, Lab Chip 14 (2014) 1074–1082.

[4] D.A. Keane, K.G. McGuigan, P.F. Ibáñez, M.I. Polo-López, J.A. Byrne, Solar photocatalysis for water disinfection: materials and reactor design, Catal. Sci. Technol. 4 (2014) 1211–1226.

[5] M. Kong, Y. Li, X. Chen, T. Tian, P. Fang, F. Zheng, X. Zhao, Tuning the relative concentration ratio of bulk defects to surface defects in TiO_2 nanocrystals leads to high photocatalytic efficiency, J. Am. Chem. Soc. 133 (2011) 16414–16417.

[6] Z. Meng, X. Zhang, J. Qin, A high efficiency microfluidic-based photocatalytic microreactor using electro spun nanofibrous TiO_2 as a photocatalyst, Nanoscale 5 (2013) 4687–4690.

[7] H. Jayamohan, Y.R. Smith, L.C. Hansen, S.K. Mohanty, B.K. Gale, M. Misra, Anodized titania nanotube array microfluidic device for photocatalytic application: experiment and simulation, Appl. Catal. B: Environ. 174–175 (2015) 167–175.

[8] L. Li, R. Chen, X. Zhu, H. Wang, Q. Liao, D. Wang, Optofluidic microreactors with TiO_2-coated fiberglass, Appl. Mater. Interfaces 5 (2013) 12548–12553.

[9] Z. Han, J. Li, W. He, S. Li, Z. Li, J. Chu, Y. Chen, A microfluidic device with integrated ZnO nanowires for photodegradation studies of methylene blue under different conditions, Microelectron. Eng. 111 (2013) 199–203.

[10] Y. Kikutani, A. Hibara, K. Uchiyama, H. Hisamoto, M. Tokeshi, T. Kitamori, Pile-up glass microreactor, Lab Chip 2 (2002) 193–196.

[11] N. Wang, L. Lei, X.M. Zhang, Y.H. Tsang, Y. Chen, H.L.W. Chan, A comparative study of preparation methods of nanoporous TiO_2 films for microfluidic photocatalysis, Microelectron. Eng. 88 (2011) 2797–2799.

[12] C. Lizama, J. Freer, J. Baeza, H. Mansilla, Optimized photodegradation of reactive Blue 19 on TiO_2 and ZnO suspensions, Catal. Today 76 (2002) 235–246.

[13] D. Daneshvara, D. Salarib, A.R. Khataee, Photocatalytic degradation of azo dye acid red 14 in water on ZnO as an alternative catalyst to TiO_2, J. Photoch. Photobio. A 162 (2004) 317–322.

[14] A.A. Khodja, T. Sehihi, J. Pilichowski, P. Boule, Photocatalytic degradation of 2-phenylphenol on TiO_2 and ZnO in aqueous suspensions, J. Photoch. Photobio. A 141 (2001) 231–239.

[15] G. Marci, V. Augugliaro, M.J. López-Muñoz, C. Martin, L. Palmisano, V. Rives, M. Schiavello, R.J.D. Tilley, A.M. Venezia, Preparation characterization and photocatalytic activity of polycrystalline ZnO/TiO_2 systems. 1. surface and bulk characterization, J. Phys. Chem. B 105 (2001) 1026–1032.

[16] I.A. Khattab, M.Y. Ghaly, L. Österlund, M.E.M. Ali. J.Y. Farah, F.M. Zaher, M.I. Badawy, Photocatalytic degradation of azo dye Reactive Red 15 over synthesized titanium and zinc oxides photocatalysts: a comparative study, Desalin. Water Treat. 48 (2012) 120–129.
[17] L. K. Adams, D.Y. Lyon, P.J.J. Alvarez, Comparative eco-toxicity of nanoscale TiO_2, SiO_2, and ZnO water suspensions, Water Res. 40 (2006) 3527–3532.
[18] L.E. Greene, M. Law, D.H. Tan, M. Montano, J. Goldberger, G. Somorjai, P. Yang, General route to vertical ZnO nanowire arrays using textured ZnO seeds, Nano Lett. 5 (2005) 1231–1236.
[19] J. Joo, B.Y. Chow, M. Prakash, E.S. Boyden, J.M. Jacobson, Face-selective electrostatic control of hydrothermal zinc oxide nanowire synthesis, Nat. Mater. 10 (2011) 596–601.
[20] G. Kenanakis, N. Katsarakis, Light-induced photocatalytic degradation of stearic acid by c-axis oriented ZnO nanowires, Appl. Catal. A: Gen. 378 (2010) 227–233.
[21] C. Ye, Y. Bando, G. Shen, D. Golberg, Thickness-dependent photocatalytic performance of ZnO nanoplatelets, J. Phys. Chem. B 110 (2006) 15146–15151.
[22] G. Kenanakis, M. Pervolaraki, J. Giapintzakis, N. Katsarakis, The use of pulsed laser deposited seed layers for the aqueous solution growth of highly oriented ZnO nanowires on sapphire substrates at 95 °C: study of their photocatalytic activity in terms of octadecanoic (stearic) acid degradation, Appl. Catal. A: Gen. 467 (2013) 559–567.
[23] G. Kenanakis, D. Vernardoub, N. Katsarakis, Light-induced self-cleaning properties of ZnO nanowires grown at low temperatures, Appl. Catal. A: Gen. 411–412 (2012) 7–14.
[24] O. Akhavan, M. Mehrabian, K. Mirabbaszadeh, R. Azimirad, Hydrothermal synthesis of ZnO nanorod arrays for photocatalytic inactivation of bacteria, J. Phys. D: Appl. Phys. 42 (2009) 225305–225314.
[25] I.S. Jeong, J.H. Kim, S. Im, Ultraviolet-enhanced photodiode employing n-ZnO/p-Sin-ZnO/p-Si structure, Appl. Phys. Lett. 83 (2003) 2946–2948.
[26] S. Xu, Z.L. Wang, One-dimensional ZnO nanostructures: solution growth and functional properties, Nano Res. 4 (2011) 1013–1098.
[27] A.A.A. Ahmed, Z.A. Talib, M.Z. Hussein, A. Zakaria, Improvement of the crystallinity and photocatalytic property of zinc oxide as calcination product of Zn–Al layered double hydroxide, J. Alloy Compd. 539 (2012) 154–160.
[28] D. Li, H. Haneda, Morphologies of zinc oxide particles and their effects on photocatalysis, Chemosphere 51 (2003) 129–137.
[29] Z. Liu, X. Zhang, S. Nishimoto, M. Jin, D.A. Tryk, T. Murakami, A. Fujishima, Highly ordered TiO_2 nanotube arrays with controllable length for photoelectrocatalytic degradation of phenol, J. Phys. Chem. C 112 (2008) 253–259.
[30] P. Déjardin, E.N. Vasina, An accurate simplified data treatment for the initial adsorption kinetics in conditions of laminar convection in a slit: application to protein adsorption, Colloids Surf. B: Biointerfaces 33 (2004) 121–127.
[31] E.N. Vasina, P. Déjardin, Adsorption of r-chymotrypsin onto mica in laminar flow conditions. Adsorption kinetic constant as a function of tris buffer concentration at pH 8.6, Langmuir 20 (2004) 8699–8706.
[32] H. Tajizadegan, O. Torabi, A. Heidary, M.H. Golabgir, A. Jamshidi, Study of methyl orange adsorption properties on ZnO–Al_2O_3 nanocomposite adsorbent particles, Desalin. Water Treat. 57 (2016) 12324–12334.
[33] J. Brash, P.W. Wojciechowski, Interfacial Phenomena and Bioproducts, Marcel Dekker Press, New York, 1996, pp. 219–222.
[34] K. Ahmed, M.N. Jones, The effect of shear on the desorption of liposomes adsorbed to bacterial biofilms, J. Lipos. Res. 13 (2003) 187–197.
[35] M.E. Davis, R.J. Davis, Fundamentals of Chemical Reaction Engineering, McGraw-Hill, New York, 2003, pp. 173–174.
[36] Y. Liu, Z.H. Kang, Z.H. Chen, Synthesis, characterization, and photocatalytic application of different

ZnO nanostructures in array configurations, Cryst. Growth Des. 9 (2009) 3222–3227.